Contents lists available at ScienceDirect

Applied Catalysis B: Environment and Energy

Phosphorus-substituted atomically dispersed Rh-N$_3$P$_1$ sites for efficient promotion in CO$_2$ hydrogenation towards ethanol production

Ke Zheng, Yufeng Li, Bing Liu, Jie Chen, Yuebing Xu, Zaijun Li, Xiaohao Liu [*]

Department of Chemical Engineering, School of Chemical and Material Engineering, Jiangnan University, Wuxi 214122, China

ABSTRACT

Ethanol synthesis through CO$_2$ hydrogenation has shown great promise in contributing to carbon neutrality. Herein, we for the first time present the phosphorus-substitution of atomically dispersed Rh-N$_4$ sites for the title reaction. The as-formed Rh-N$_3$P$_1$ sites enable the reaction product notably switching from nearly total methanol (91.3%) towards major ethanol (81.8%) with a high TOF of 420.7 h^{-1}. This outstanding promotion in both ethanol formation and CO$_2$ conversion (69% higher) could be assigned to the donation of electron from P atom effectively weakening C-O bond in CH$_3$OH*, facilitating its cleavage into CH$_3$*, and enabling the coupling between CO* and CH$_3$*. The presence of Rh-P site pair assists C-O bond activation with a longer bond length owing to a strong affinity of P atom to O atom in CH$_3$OH*. This research underscores the importance of tuning the coordination and electronic environment of active metal sites for site pair synergistic catalysis.

1. Introduction

Given the substantial consumption of chemical fuels and the excessive release of the greenhouse gas CO$_2$ into the atmosphere, fuel shortage and environmental problems have seriously affected the survival and development of human society [1,2]. Therefore, the capture and utilization of CO$_2$ has become a prominent research focus. As a safe and renewable C1 resource, the activation and hydrogenation of CO$_2$ to produce valuable chemicals, such as carbon monoxide [3–5], methane [6–8], olefins [9–11], aromatics [12–14], and alcohols [15–20], hold significant importance in achieving carbon neutrality and promoting the development of a circular economy. Among these chemicals, ethanol (EtOH) plays a pivotal role in various aspects of daily life, including medicine, cosmetics, and fuel additives. Ethanol is also an important chemical raw material and can be transformed into other chemicals, such as ethylene [21] and its derivative [22]. Currently, ethanol is primarily produced through grain fermentation, which not only depletes food resources but also lacks environmental sustainability. Therefore, developing synthetic gas (CO$_2$/H$_2$) to produce ethanol holds tremendous promise. However, since CO$_2$ is a thermodynamic stable and chemically inert molecule, and the formation of ethanol requires C-C coupling, which is challenging to control owing to uncontrollable polymerization, both of them lead to directly converting CO$_2$ into ethanol with excellent catalytic performance still remains a tough challenge [23].

In recent years, significant works have been devoted to convert CO$_2$ hydrogenation into ethanol [24–26], including nobel metal-based [27–29], Co-based [30,31], Cu-based [32], Fe-based [33–35], and multi-element composite catalyst [36,37]. Among them, Rh-based catalysts have attached widespread attention in selective ethanol production [38–40]. Nevertheless, the high cost of Rh limits its practical application, necessitating strategies to maximize its utilization. Single-atom catalysts (SACs) have garnered significant attention due to their fully exposed active metal atoms dispersed on the support, leading to a 100% atom utilization efficiency and making them highly desirable for catalytic applications [41–43]. SACs have been extensively investigated in catalyzing the conversion of CO$_2$ to various chemicals, including carbon monoxide, methane, methanol, dimethyl ether, formic acid, ethene, and ethanol, etc [44]. Among them, several noble metal-based SACs have exhibited exceptional catalytic performance in CO$_2$ hydrogenation to produce ethanol, such as Rh$_1$/CeTiO$_x$ [45], Ir$_1$/In$_2$O$_3$ [46], and 0.1%Pd/Fe$_3$O$_4$ [47], etc.

Recently, the unique pore characteristics of MOFs and their derived carbon-based nanomaterials have captured considerable interest in the field of catalysis, which can effectively confine metal nanoparticles within the pores. By using the molecular channels of MOFs as "cages" to encapsulate and anchor mononuclear metal precursors, their uniform spatial distribution and atomic level dispersion can also be achieved [48]. Zinc-based zeolite imidazole salt frameworks (ZIF-8) is a typical

---

MOF material with abundant pore cage, large specific surface area, and controllable pore structure [49]. After high-temperature pyrolysis under inertness atmosphere, ZIF-8 can be converted into nitrogen-doped porous carbon materials. The doped N sites are favorable for the anchoring of metal atoms, leading to the formation of stable SACs [50, 51]. The metal sites are the reaction centers for reactants activation, and their properties depend on the electronic structure and coordination environment [52]. The coordination structure of active metal sites in SACs has been recognized as a key factor in tailoring their catalytic performance. Huang et al. found that adjusting the coordination number of Cu single atom site (Cu-N$_3$ and Cu-N$_4$) can affect the products selectivity in CO$_2$ hydrogenation [53]. Besides, it is found that heteroatoms (B [54], S [55], P [56,57], etc.) doped carbon could regulate the structures of active center. However, to our knowlegement, limited attention has been given to elucidating the influence of coordination structure of active metal sites on CO$_2$ activation and reaction pathway in CO$_2$ hydrogenation over N-doped carbon supported SACs.

In this study, we developed a Rh-N$_3$P$_1$ site by phosphorus-substitution of atomically dispersed Rh-N$_4$ sites. Rh/CN catalyst with Rh-N$_4$ sites exhibits a nearly total methanol selectivity of up to 91.3%. However, the resulting Rh/CNP catalyst with Rh-N$_3$P$_1$ sites enables the reaction product obviously to switch from methanol to ethanol with about 81.8% selectivity and a TOF of 420.7 h^{-1}, surpassing the performance of most catalysts shown in previous studies. Comprehensive characterizations, including XANES, EXAFS, in situ XPS, model reaction testing and theorical calculations, have provided insights into the role of phosphorus in tailoring the coordination structure of Rh active metal sites, which is highly related to the activation of C-O bonds in CH$_3$OH* and the reaction pathway in CO$_2$ hydrogenation. This work highlights the significance of tuning active metal sites coordination environment for optimizing catalytic performance in CO$_2$ hydrogenation processes.

2. Experimental

2.1. Catalyst preparation

2.1.1. Synthesis of Rh/CNP catalyst

Firstly, 2-methylimidazole (2.62 g) was dissolved in 60 mL of methanol with continuous stirring to obtain solution A. In the preparation of solution B, PPh$_3$ (1.829 g), Zn(NO$_3$)$_2$·6 H$_2$O (2.38 g), and Rh (NO$_3$)$_3$·6 H$_2$O (0.073 g) were dissolved in 30 mL of methanol with continuous stirring. Subsequently, solution A was quickly added to solution B and stirred for 30 min at room temperature. The resulting mixture was then transferred into a stainless steel autoclave and placed in an oven, maintaining a temperature of 120 °C for 4 h. The hydrothermal product was filtered and washed with methanol for 3 times, and then dried at 70 °C under vacuum for 12 h. Finally, the sample was calcined at 950 °C for 3 h in a N$_2$ atmosphere to produce the Rh/CNP catalyst. For comparison, 0.915 and 7.316 g PPh$_3$ were used for the preparation of Rh/CNP-L and Rh/CNP-H, where the "H" and "L" represented "High" and "Low", respectively. In addition, 0.037 and 0.365 g Rh(NO$_3$)$_3$·6 H$_2$O were used for the preparation of 0.05% Rh/CNP and 0.58% Rh/CNP, respectively.

2.1.2. Synthesis of Rh/CN catalyst

Rh/CN catalyst was synthesized by the similar process with Rh/CNP but without the addition of PPh$_3$.

2.1.3. Synthesis of M/CN and M/CNP catalysts

M/CN and M/CNP (M = Pd, Ir, Co, and Cu) catalysts were synthesised by replacing Rh(NO$_3$)$_3$·6 H$_2$O with corresponding metal precursor, including Pd(NO$_3$)$_2$, H$_2$IrCl$_6$·xH$_2$O, Co(NO$_3$)$_2$·6 H$_2$O, and Cu (NO$_3$)$_2$·3 H$_2$O.

2.1.4. Synthesis of referenced catalysts

5%Zn-Rh/CN and 5%Zn-Rh/CNP catalysts were prepared using an incipient wetness impregnation method. In detail, desired amounts of Zn (NO$_3$)$_2$·6 H$_2$O were impregnated to the Rh/CN and Rh/CNP. After impregnation, the samples were dried in vacuum at 80 °C for 12 h. Then, the samples were calcined at 400 °C for 2 h. The obtained catalysts were denoted as 5%Zn-Rh/CN and 5%Zn-Rh/CNP, respectively. Additionally, Rh/CN and Rh/CNP catalysts were treated with NH$_3$·H$_2$O to remove a portion of Zn. As a typical run, 1 g catalyst was dispersed in 20 mL of NH$_3$·H$_2$O (25 wt%). The mixture was stirred at room temperature overnight. After filtrating, washing with water, drying, and calcining in the N$_2$ at 400 °C for 2 h. The obtained catalysts were denoted as Rh/CN-NH$_3$ and Rh/CNP-NH$_3$, respectively.

2.2. Catalyst characterization

X-ray diffraction (XRD) measurement was conduced on an AXS D2 ADVANCE diffractometer (Brucker), which was equipped with Cu Kα radiation (λ = 0.15418 nm). The diffraction angles were scanned from 10 to 80° (2θ) with the step size of 0.02°. Raman spectra were obtained using a InVia instrument (Renishaw), utilizing a 532 nm laser line. N$_2$ physiorption was performed using Quantachrome Autosorb iQ instrument. Scanning electron microscope (SEM) images were acquired using an S-4800 field emission scanning electron microscope from Japan Hitachi. Transmission electron microscopy (TEM) images were acquired from an FEI Talos F200S microscope with a accelerating voltage of 200 kV. High-angle annular dark-field scanning-transmission electron micrographs (HAADF-STEM) and the corresponding energy-dispersive X-ray spectroscopy (EDX) elemental mappings were performed using a super XG1 analysis system. Aberration-corrected high-angle annular dark-field scanning-transmission electron micrographs (AC-HAADF-STEM) were obtained on FEI Themis Z microscope. The elemental analysis of the catalyst was carried out using the inductively coupled plasma optical emission spectroscopy (ICP-OES) with a PerkinElmer Avio 200 Optical Emission Spectrometer. In situ XPS measurements were performed on ThermoFischer ESCALAB 250Xi instrument, employing monochromated Al Kα (hν = 1486.6 eV) as the exciting source at 12.5 kV and 16 mA. The samples underwent the reducing pretreatment with 10% H$_2$/Ar at 300 °C for 1 h within the analyzer chamber, following by evacuation and the XPS tests. The peak positions for each element were calibrated according to binding energy of C1s at 284.6 eV. X-ray absorption near edge structure (XANES) and extended X-ray absorption fine structure (EXAFS) of Rh K-edge were measured using the XAS station (BL14B2) of Super Photon ring-8 in Japan. The storage ring electron beam energy was set as 8 GeV, along with the monochromatized incident X-ray from Si (311) double-crystal. The results were collected from a solid-state detector at normal temperature and pressure. The calculation of the coordination number was achieved according to the fixed S$_0^2$ values derived from Rh foil.

H$_2$-D$_2$ exchange experiments were performed on a chemisorption analyzer (Microtrac BELCAT II). The catalyst, weighing 150 mg, was subjected to pre-treatment at 300 °C for 1 h in a 5% H$_2$/N$_2$ atmosphere (30 mL/min) and subsequently cooled to 100 °C under an Ar flow. Subsequently, 0.98 mL of a mixed gas containing H$_2$ and D$_2$ in a 1:1 ratio, carried by Ar, was introduced into the reactor during each pulse. Temperature-programmed desorption (TPD) measurements (CO$_2$-TPD and CO-TPD) were conducted using a same process. In terms of CO$_2$-TPD, before the measurements, 150 mg catalyst was subjected to reduction in 5% H$_2$/N$_2$ flow of 30 mL/min at 300 °C for 1 h. After cooling down to 50 °C in Ar flow, a flowing 10% CO$_2$/Ar flow of 30 mL/min was introduced for 1 h. Then, the physically adsorbed CO$_2$ was removed by a flowing pure He for 30 min. Finally, the CO$_2$-TPD profiles were obtained by increasing the temperature up to 800 °C (10 °C/min).

CO-adsorbed in-situ diffuse reflectance infrared Fourier transform spectroscopy of (in situ CO-DRIFTS) measurements were performed on a Bruker VERTEX 80/80 v. After loading the catalyst into the cell, it was pretreated at 300 °C for 1 h under a 5% H$_2$/N$_2$ flow. After cooling the sample to room temperature in a He atmosphere, it was purged in a He

flow for 30 min, and the background spectrum was recorded. Subsequently, the sample was exposed to a 1% CO/Ar for 30 min until saturation. Afterward, the sample underwent a 30 min purge with He to eliminate any gas-phase CO. Finally, the DRIFT spectrum was obtained with 64 scans at a resolution of 4 cm^{-1}. In situ DRIFT spectra were recorded on a Nicolet 5700 spectrometer featuring a mercury cadmium telluride (MCT) detector, offering a resolution of 4 cm^{-1}. Prior to the measurement, the sample underwent pretreatment in a 5% H$_2$/N$_2$ atmosphere (30 mL/min) at 300 °C for 1 h. Subsequently, it was cooled to 50 °C in an Ar flow and purged with Ar for 30 min. The spectra were recorded as the mixed gas (CO$_2$/H$_2$/H$_2$O) switched into the testing cell under the desired temperatures.

2.3. Computational details

In this study, all theoretical calculations were conducted using the Vienna Ab Initio Simulation Package (VASP 5. 4. 4) [58]. The Projector Augmented Wave (PAW) pseudopotential method was employed to describe the interaction between nuclei and electrons [59]. A cut-off energy of 400 eV was used, and the exchange and correlation energies were computed using the Perdew-Burke-Ernzerhof (PBE) approach [60]. As for structural optimization, the convergence criteria for force and energy were established as 0.03 eV/Å and 10^{-5} eV, respectively. The transition state energy was determined using the climbing image nudged elastic band (CI-NEB) method [61]. Similar to the previous study [62, 63], the N-doped and N- and P-doped carbon model was built in the following procedure. A graphene structure containing 32 carbon atoms with a vacuum layer of 15 Å was first created. Then, two adjacent carbon atoms were removed to expose four carbon vacancy atoms. Next, these four carbon atoms were replaced by four N atoms or three N atoms and one P atom, following by structural optimization to obtain CN and CNP models, respectively. Finally, one Rh atom was boned to the four N atoms or three N atoms and one P atom, following structural optimization to obtain Rh/CN and Rh/CNP models, respectively.

2.4. Catalytic test

2.4.1. Catalytic test in the batch reactor

The CO$_2$/CO hydrogenation reaction was carried out in a 100 mL stainless-steel autoclave, which was similar to that used previously [45]. Prior to reaction, the catalyst was reduced in a flowing H$_2$ of 30 mL/min at 300 °C and 0.1 MPa for 1 h. In a standard experiment, 30 mg catalyst and 20 mL water were introduced into the reactor. The reactor was then sealed and purged 3 times with 1 MPa reactant gas (24.16%CO$_2$/72.69% H$_2$/3.25%N$_2$ or 31.95%CO/64.05%H$_2$/4%N$_2$) to remove the inside air, followed by filling with reactant gas to the desired gas pressure. The reactor was heated to the target reaction temperature, and the reaction was started with stirring at a speed of 400 rpm, lasting for 5 h. After cooling the reactor in an ice water bath, the gas composition, which included H$_2$, N$_2$, CO, CO$_2$, and CH$_4$, was analyzed online using Agilent GC 7820 A gas chromatographs equipped with a thermal conductivity detector (TCD) coupled with both a Porapak Q column and a 5 Å molecular sieve column. The liquid product was obtained after centrifugation, which was mixed with D$_2$O containing tris(trimethylsilyl) phosphate (TMSP) as the internal standard and then analyzed by ^{1}H NMR spectroscopy (Bruker AVANCE III HD 400 spectrometer). In the catalyst reuse experiment, the spent solid catalyst was obtained by centrifugation, washed with deionized water, dried at 80 °C for 2 h, and then used directly for the subsequent run. CO$_2$ conversion and product selectivity were determined using the following equations:

$$CO_2 \ conversion \ = \ \frac{[CO_2]_b \ - \ [CO_2]_a}{[CO_2]_b} \ \times \ 100\% \qquad (1)$$

$$Selectivity \ of \ C_i \quad (\%) = \ \frac{C_i \times i}{[CO_2]_b - [CO_2]_a} \qquad (2)$$

where the [CO$_2$]$_b$ and [CO$_2$]$_a$ represent the molar amount of CO$_2$ before and after reaction, respectively. C$_i$ represents the molar amount of the product, and i represents the number of carbon atom in C$_i$. Note that after the reaction, CO$_2$ exists both in gas phase and liquid phase. These two parts both contribute to [CO$_2$]$_a$. The molar amount of CO$_2$ in the gas phase (denoted as [CO$_2$]$_{ag}$) is directly detected by GC using the N$_2$ as an internal standard, while that in the liquid phase (denoted as [CO$_2$]$_{al}$) is obtained from the blank test. In detail, the CO$_2$ hydrogenation reaction is performed only without the addition of catalysts. Then, the reactor is cooled down in the ice water bath. After that, the molar amount of the unreacted CO$_2$ (denoted as [CO$_2$]$_{ag-blank}$) in the gas phase is directly detected by GC and [CO$_2$]$_{al}$ is calculated by the eqution: [CO$_2$]$_{al}$ = [CO$_2$]$_b$ - [CO$_2$]$_{ag-blank}$.

The TOF in this work is calculated by the equation as follows:

$$TOF = \ \frac{X_{CO_2} \times S_{ethanol} \times n_{CO_2}}{t \times (m_{catal} \times N_{Rh}/M_{Rh})} \qquad (3)$$

where X$_{CO_2}$ represents the CO$_2$ conversion, S$_{ethanol}$ denotes the ethanol selectivity, n$_{CO_2}$ stands for the amount of CO$_2$, t represents the reaction time, m$_{catal}$ is the mass of catalyst, N$_{Rh}$ is the metal content of Rh, and M$_{Rh}$ corresponds to the relative atomic mass of Rh.

2.4.2. Catalytic test in the fixed-bed reactor

The catalytic reaction tests were conducted in a high-pressure continuous-flow fixed-bed reactor with an internal diameter of 8 mm. A mixture of 0.1 g catalyst and 1.0 g quartz sand was evenly prepared. Before the reaction, the catalyst underwent reduction in a H$_2$ flow (30 mL/min) at 300 °C and 0.1 MPa for 1 h. The detailed evaluation and calculation methods are shown in our previous publication [27].

2.4.3. Hydroformylation reaction performance test

The hydroformylation experiments were conducted in a 30 mL stainless steel autoclave equipped with a magnetic bar. 100 mg catalyst, 10 mmol 1-hexene, and 10 mL n-heptane were added into the reactor. The autoclave was pressurized with syngas (48%CO/48%H$_2$/4%N$_2$) to a pressure of 5.0 MPa. Subsequently, the autoclave was heated to 100 °C for 24 h with a stirring speed of 500 rpm. After reaction, the reactor was cooled down in the ice water bath. The reactant solution was analyzed using gas chromatography (SHIMADZU GC-2014 with an HP-1 column) and n-butanol was used as an internal standard. 1-hexene conversion and product selectivity were determined using the following equations:

$$1 - hexene \ conversion \ = \ \frac{[1 - hexene]_b \ - \ [1 - hexene]_a}{[1 - hexene]_b} \ \times \ 100\% \qquad (4)$$

$$Selectivity \ (\%) = \ \frac{n_i}{n_{linear-heptanal} + n_{branched-heptanal} + n_{internal \ olefins}} \qquad (5)$$

where the [1-hexene]$_b$ and [1-hexene]$_a$ represent the molar amount of 1-hexene before and after reaction, respectively. n$_i$ is the molar amount of the product (linear-heptanal, branched-heptanal, or internal olefins).

3. Results and discussion

3.1. Synthesis and structural characterizations of the catalysts

Rh/CNP was prepared via wet-chemical combined with pyrolysis method, the synthesis procedure is shown in Fig. 1a. ZIF-8 features a pore size of 3.4 Å and a cavity diameter of 11.6 Å, making it suitable for encapsulating the triphenylphosphine (PPh$_3$, 8.9 Å) through microporous confinement effect (Fig. S1). Rh(NO$_3$)$_3$ was mixed with PPh$_3$ and Zn (NO$_3$)$_2$, and 2-methylimidazole. After the self-assembly process, PPh$_3$ was trapped in one ZIF-8 cage, denoted as Rh/PPh$_3$ @ZIF-8. The XRD pattern of Rh/PPh$_3$ @ZIF-8 revealed no change compared with that of Rh/ZIF-8 (Fig. S2a), both them are well matched with that of ZIF-8. There is no Rh-related diffraction peaks observed, suggesting the
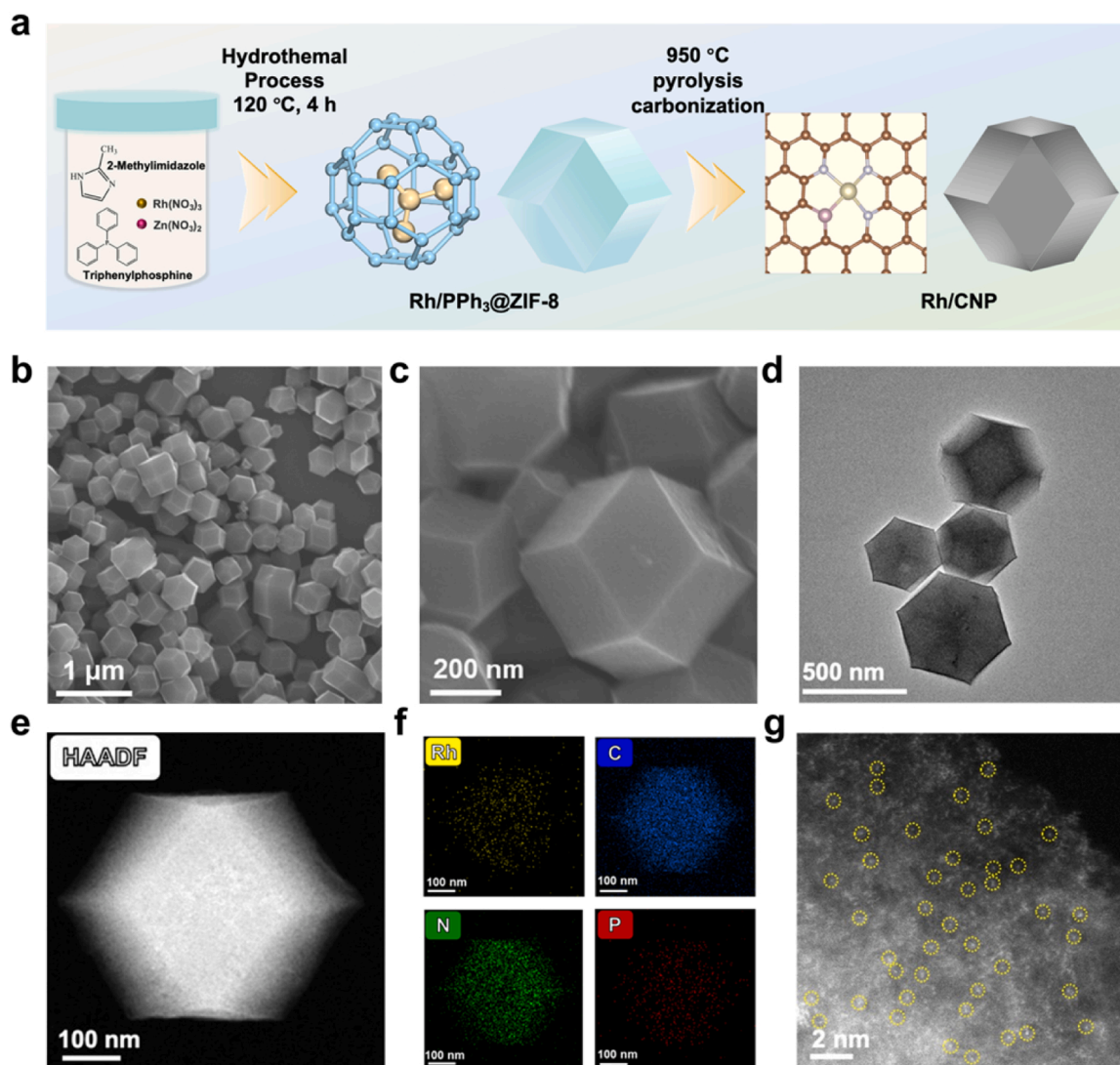
Fig. 1. (a) Schematic illustration of the formation of Rh/CNP, (b, c) SEM and (d) TEM images of Rh/CNP, (e) HAADF-STEM image and (f) corresponding EDS mappings of Rh/CNP sample, and (g) AC-HAADF-STEM image of Rh/CNP sample.

homogeneous distribution of Rh species. After pyrolysis at 950 °C under N_2 atmosphere, $Rh(NO_3)_3$ underwent reduction through the carbonization of the organic linker, leading to the formation of single Rh atoms anchored on N_3P_1 sites formed through phosphorus-substitution of N_4 sites (denoted as Rh/CNP). PPh_3 @ZIF-8 serves as a molecular enclosure, effectively spatially isolating the $Rh(NO_3)_3$. Meanwhile, the N_3P_1 sites that form in situ also offer a plentiful supply of coordination sites for stabilizing the Rh single atom. The phosphorus-free Rh/CN catalyst was prepared using a similar process to Rh/CNP but without the addition of PPh_3. Based on the results from the ICP-OES analysis (Table S1), the Rh contents in Rh/CNP and Rh/CN were determined to be 0.09 and 0.07 wt%, respectively, and the P loading in Rh/CNP was 1.43 wt%. The XRD patterns of Rh/CNP and Rh/CN displayed the broad shoulder peaks at $2\theta \approx 25°$ and $44°$, which were attributed to the (002) and (101) planes of the graphitic carbon [50], suggesting that PPh_3 @ZIF-8 and ZIF-8 were converted to graphitic-like material (Fig. S2b), and that can be further confirmed by Raman spectroscopy. From Fig. S3, the D band found at approximately 1340 cm^{-1}, was attributed to structural defects in the graphitic structure [64]. Meanwhile, the G band, situated at around 1580 cm^{-1}, represented the degree of graphitization in the carbon material [64]. Typically, the peak intensity ratio of the D to G band (I_D/I_G) is utilized to quantify the extent of structural defects in the graphitic structure [65]. The I_D/I_G value slightly increased from 0.98 for Rh/CN to 1.03 for Rh/CNP, indicating the surface defects slightly increased after the modification of P. Brunauer-Emmett-Teller (BET) adsorption-desorption method was performed to investigate the porous structure of the samples (Fig. S4, Table S2). Rh/CNP shows higher BET specific surface area of 520.8 m^2g^{-1} than that of Rh/CN (461.2 m^2g^{-1}). An increase in the BET specific surface area can expose more active sites, facilitating the adsorption of reactants and products.

The morphology and microstructure of the samples were examined. From SEM (Figs. 1b and 1c, Fig. S5) and TEM (Fig. 1d, Figs. S6a and S6b) images, the as-prepared Rh/CNP and Rh/CN catalysts both exhibited well structural integrity rhombic dodecahedron-shaped morphology. Interestingly, with introducing P into the Rh/CN catalysts, the size of Rh/CNP was obviously decreased from about 3–4 μm to about 500 nm. On the one hand, the introduction of PPh_3 might dilute the proportion of 2-methylimidazole and $Zn(NO_3)_2 \cdot 6 H_2O$. On the other hand, the presence of PPh_3 might have coordination effect with Zn^{2+} to form $[PPh_3Zn]^{2+}$, which had steric effect on the coordination reaction between Zn^{2+} and 2-methylimidazole and slowed down the growth of ZIF-8 crystals. HAADF-STEM images and corresponding EDS mappings reveal a uniform distribution of Rh, C, N, P (Figs. 1e and 1f) and no Rh clusters were observed. Similarly, the Rh, C, and N elements are uniformly distributed within the carbon matrix in the Rh/CN sample (Figs. S6c-f). AC-HAADF-STEM was employed to gather atomic-level

information of Rh/CNP. Fig. 1g reveals the bright dots, which can be attributed to isolated metal atoms, providing confirmation of the single-atom distribution of Rh in Rh/CNP.

3.2. Electronic state and coordination structure of the catalysts

XANES and EXAFS at Rh K-edge were conducted to further explore the structure of Rh/CN and Rh/CNP catalysts in atomic level (Fig. S7). XANES was conducted to examine the chemical state of the samples. Fig. 2a displays the Rh K-edge XANES spectra for Rh/CN, Rh/CNP, as well as reference samples of Rh foil and Rh_2O_3. Comparing the adsorption edge positions in the XANES spectra with those of reference samples, the oxidation states of Rh in Rh/CN and Rh/CNP are revealed. Extended Fourier transform (FT) EXAFS spectra of Rh/CN and Rh/CNP both exhibited a notable peak at approximately 1.59 Å, which corresponds to Rh-N scattering paths (Fig. 2b). Moreover, FT of Rh/CNP reveals an additional peak at ~1.93 Å, which corresponds to Rh-P scattering paths. The Rh-Rh path at ~2.39 Å for Rh foil standards was not observed in Rh/CN and Rh/CNP, confirming the presence of Rh

single atom in Rh/CN and Rh/CNP. Additionally, the wavelet transform (WT) of Rh K-edge EXAFS oscillations was examined to provide additional confirmation of the atomic monodispersity of Rh species [66]. In Fig. 2c, the WT contour plots of Rh/CN and Rh/CNP displayed the intensity maximum at about 4.2 Å that can be assigned to Rh-N/P contributions. There is no peak at ~8.5 Å that ascribed to Rh-Rh bond can be found, validating the atomically dispersed Rh. According to Table S3, the coordination number of Rh-N bond in Rh/CN is about 4.0, illustrating that Rh atom was coordinated with four N atoms (Fig. S8a). The coordination number of Rh-N in Rh/CNP is approximately 3.2, while that of Rh-P is around 1.1. This suggests that the Rh atom is coordinated with three N atoms and one P atom. The structure of Rh/CNP, as shown in Fig. S8b, illustrates that one of the N atoms adjacent to Rh has been replaced by a P atom, resulting in a change in the coordination structure and electron density around Rh.

Infrared (IR) spectroscopy by using CO adsorption as probe is a powerful technique to explore the properties of active sites. As shown in Fig. 2d, two dominant CO frequencies were observed at 2082 and 2014 cm^{-1} on the Rh/CN sample, which generally correspond to
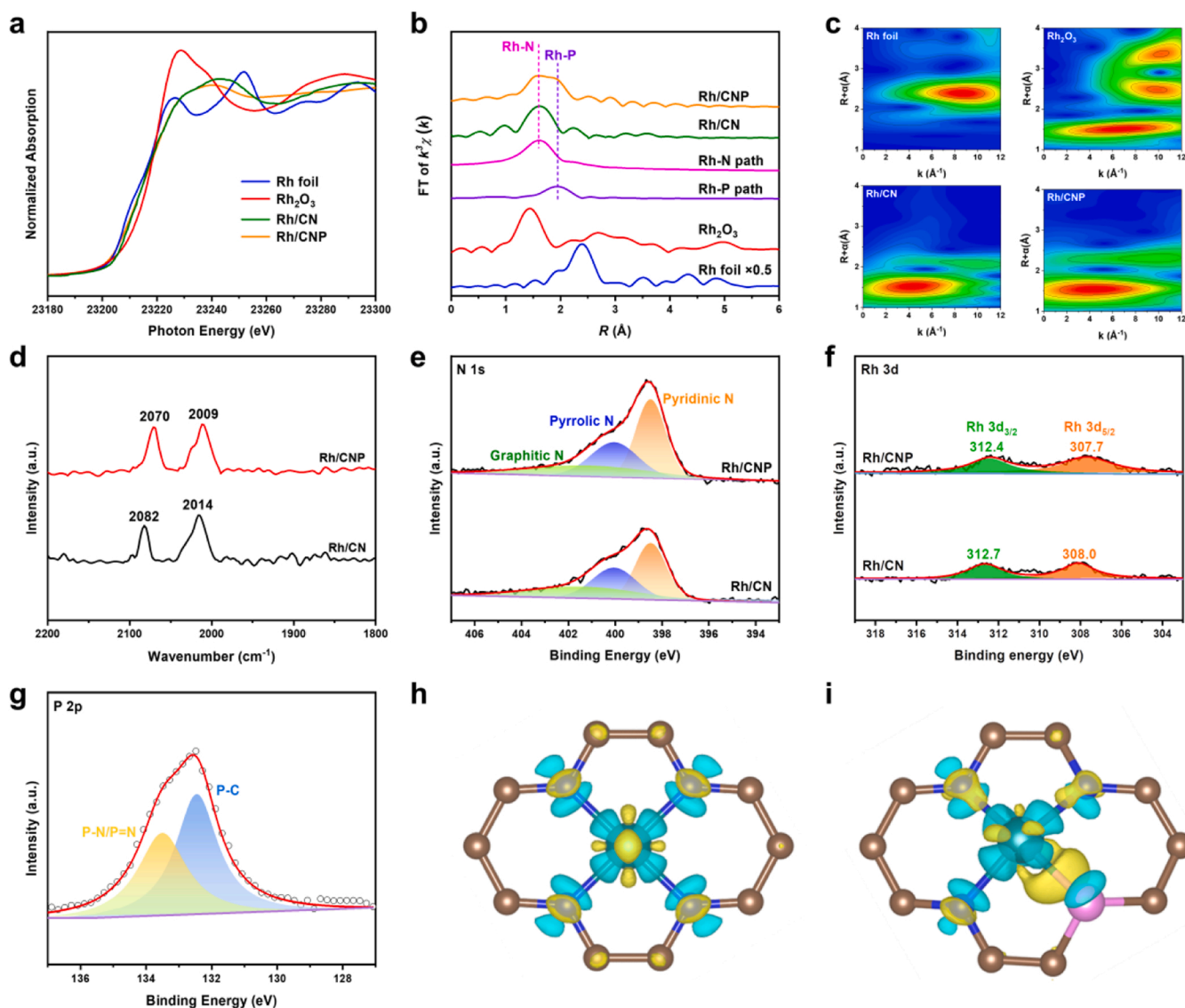

Fig. 2. (a) XANES and (b) EXAFS spectra of Rh K-edge of Rh/CN, Rh/CNP, and references, (c) WT EXAFS of the Rh K-edge, (d) In situ CO-DRIFTS of Rh/CN and Rh/CNP catalysts, In situ XPS survey spectra of (e) N 1 s, (f) Rh 3d, and (g) P 2p core levels in the Rh/CN and Rh/CNP samples, and charge density difference of Rh/CN (h) and Rh/CNP (i) model. The yellow and cyan colors represent the accumulation and depletion of electron density, respectively, with an iso-surface value set at 0.01 $e/bohr^3$. Rh atoms in dark cyan; C atoms in brown; N atoms in blue; P atoms in pink.

symmetric and asymmetric stretching vibrations of Rh-$(CO)_2^+$ gem-dicarbonyl species [67,68]. This suggests that the Rh species in Rh/CN are atomically dispersed. However, in the case of Rh/CNP, these two peaks were shifted to lower wavenumbers (2070 and 2009 cm^{-1}). The lower wavenumbers indicate that the C−O bond was more efficiently activated on Rh in Rh/CNP due to increased electron transfer from Rh to CO 2π antibonding orbital, resulting in a red shift in its infrared absorption peak.

In-situ XPS analysis was conducted to investigate the elemental composition and chemical state of the catalysts. The XPS spectra of the C 1 s peak (Fig. S9) were fitted into three peaks with binding energies of 284.8 eV, 286.2 eV, and 288.5 eV, which can be attributed to C=C, C=N, and C-N, respectively [69]. It suggests that successful N doping of the carbon-based materials. The N 1 s spectrum can be fitted into three peaks corresponding to graphitic N (401.6 eV), pyrrolic N (400.1 eV), and pyridinic N (398.5 eV) (Fig. 2e) [51], which served as anchoring Rh sites by coordination. Pyridinic N is reported to be advantageous for the adsorption and activation of CO_2 [3]. The Rh 3d XPS results are shown in Fig. 2f, where the peaks of Rh $3d_{5/2}$ and Rh $3d_{3/2}$ located at 308.0 and 312.7 eV were observed in the reduced Rh/CN sample, confirming the presence of Rh^+ species [29]. This result is well in accordance with that of the XANES. Interestingly, these two peaks exhibited a downward shift of approximately 0.3 eV following the substitution of atomically dispersed Rh-N_4 sites with phosphorus. This shift can be attributed to electron transfer from P to Rh, causing the electrons are enriched on Rh sites over Rh-N_3P_1 sites. To verify the role of P as an electron donor, we conducted XPS of CNP support and Rh/CNP catalyst. The P 2p XPS spectra of CNP support showed one peak that could be deconvoluted into two contributing peaks at 132.2 eV and 133.2 eV (Fig. S10). These peaks were attributed to P-C and P-N/P = N bonds, respectively [70,71]. However, Fig. 2g showed that these two peaks shifted towards the high binding energy over Rh/CNP catalyst (132.5 and 133.5 eV), indicating that the presence of Rh results in electron deficiency in P. In other words, electron transfer occurred from P to Rh.

On this basis, the Bader charges analysis and charge density difference were conducted over Rh/CN and Rh/CNP catalyst models. As shown in Fig. 2h, the Rh atom in Rh/CN was stabilized by four symmetric N atoms. The strong electronic withdraw effect of N leads to the depletion of electron density along with the direction of Rh-N bonds. However, after phosphorus-substitution of Rh-N_4 sites, the electron distribution around Rh in Rh/CNP became asymmetric due to the different electronegativity of N and P (Fig. 2i). Meanwhile, there is a large area of electron accumulation between P and Rh, which results from the electron transfer from P to Rh. According to calculated Bader charge (Table S4), more electrons depletion was found for Rh/CN (−0.6953 e) than for Rh/CNP (−0.3997 e). In other words, the substitution of P could enrich electron density of Rh, resulting in a lower valence of Rh in Rh/CNP than that in Rh/CN. This result is in accordance with XANES and XPS.

3.3. Catalytic performance of CO_2 hydrogenation

The catalytic performance in the CO_2 hydrogenation was assessed in a batch stainless-steel reactor. After reaction for 5 h, both gaseous and liquid products were analyzed. As depicted in Fig. 3a, the CO_2 conversion of Rh/CNP catalyst is 4.9%, which is 69% higher than that of Rh/CN catalyst (2.9%). Considering the different sizes of Rh/CN and Rh/CNP, we calculated the specific activity (catalyst activity/specific area) of these two catalysts. It was found that the specific activity of Rh/CNP (1.73 $\times10^{-2}$ $mmol_{CO2}$/(m^2·h)) was significantly higher than that of Rh/CN (1.15 $\times10^{-2}$ $mmol_{CO2}$/(m^2·h)), which suggested that the Rh/CNP was more conducive to the conversion of CO_2. The Rh/CN catalyst exhibited a preference for producing methanol with a selectivity of 91.3%. After phosphorus-substitution of Rh-N_4 sites, the Rh-N_3P_1 sites exhibit different catalytic behavior, which makes the main reaction product transformation from methanol to ethanol with about 81.8% selectivity. In contrast, the CN and CNP catalysts without Rh loading were found to be inactive in the reaction (Fig. S11), suggesting that the
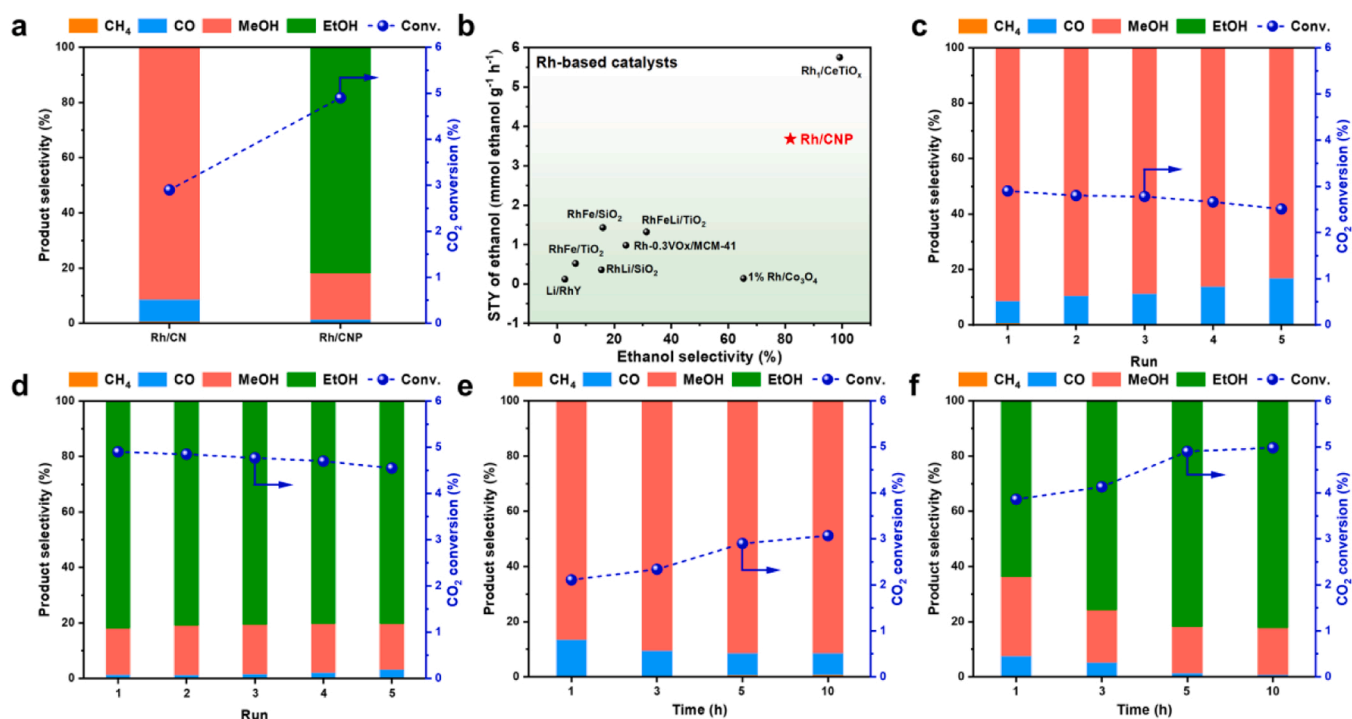

Fig. 3. (a) Comparison of the activity and selectivity over the Rh/CN and Rh/CNP catalysts, reaction conditions: catalyst (30 mg), H_2O (20 mL), 250 °C, initial pressure (3.0 MPa, $H_2/CO_2 = 3/1$), reaction time is 5 h, 400 rpm, (b) Comparing the space-time yield of ethanol obtained in this study with other Rh-based catalysts reported in the literatures, Recycled testing of Rh/CN (c) and Rh/CNP (d) catalysts for reaction of 5 h at five runs, and dependences of product selectivity and CO_2 conversion on time over Rh/CN (e) and Rh/CNP (f) catalysts, reaction conditions are same as those described in (a).

outstanding catalytic performance of Rh/CNP can be attributed to the synergistic effects between the Rh active metal sites and the CNP support. For a deeper understanding of the synergistic mechanism, a series of single atom catalyst M/CN and M/CNP (M=Pd, Ir, Co, and Cu) were synthesised by replacing Rh with other metals and the CO_2 hydrogenation performance was conducted. As shown in Fig. S12, the M/CN catalyst can only generate methanol. However, for phosphorus-substituted M/CNP catalyst, the enhanced CO_2 conversion and ethanol formation can be observed, which means that the promotional effect of P is universal. To examine the impact of P content on the catalytic performance, we prepared Rh/CNP catalysts with different P contents by adjusting the amount of PPh₃ added. 0.915 and 7.316 g PPh₃ were used for the preparation of Rh/CNP-L and Rh/CNP-H and the P content determined by ICP was 0.74 wt% and 5.64 wt%, respectively. As shown in Fig. S13, both the CO_2 conversion and ethanol selectivity are low over Rh/CNP-L catalyst, which is related to that the low content of P cannot form coordination with Rh. When the P content increases to 1.43 wt%, CO_2 conversion and ethanol selectivity significantly increase. But when the P content further increases, the CO_2 conversion and ethanol selectivity decrease over Rh/CNP-H catalyst. After collecting the spent Rh/CNP-H catalyst for the second reaction evaluation, it was found that the activity significantly decreased. It indicates that the poor catalytic performance in CO_2 hydrogenation into ethanol may be related to its unstable structure. Therefore, the optimal amount of P addition contributes to the formation of ethanol.

The pyrolysis of ZIF-8 doped with metal ions is becoming a common strategy for the synthesis of SACs. Most Zn can be removed by evaporation at high temperatures. However, as far as we know, it is difficult to design SACs that do not leave residual Zn species after pyrolysis at high temperatures. The ICP-OES results showed that the presence of Zn with similar content of about 4 wt% in both Rh/CN and Rh/CNP catalysts (Table S5), which may be related to the formation of stable Zn single atom sites in the early pyrolysis process [72]. Fig. S11 has shown that the CN and CNP supports without Rh exhibited almost no catalytic activity, indicating that the residual Zn after ZIF-8 pyrolysis is not the active sites in CO_2 hydrogenation. To further prove this result, we checked the effect of Zn concentration on catalytic performance. The 5 wt% Zn was impregnated into Rh/CN and Rh/CNP for the performance evaluation. As shown in Fig. S14, after impregnating 5 wt% Zn into the catalyst, there was no significant change in catalytic performance. In addition, the Rh/CN and Rh/CNP catalysts were treated with 25 wt% $NH_3 \cdot H_2O$ overnight to remove a portion of Zn, the obtained catalysts were denoted as Rh/CN-NH_3 and Rh/CNP-NH_3, respectively. The Zn content in the Rh/CN-NH_3 and Rh/CNP-NH_3 was significantly decreased (Table S5). However, the evaluation results were basically the same as before treatment (Fig. S14). It suggested that the residual Zn after pyrolysis will not affect the catalytic behavior of the catalyst as the single active sites or the synergistic catalysis with Rh sites.

CO_2-TPD results show that Rh/CNP exhibits enhanced CO_2 adsorption peak area in the range of 300–700 °C (Fig. S15), which indicates that Rh/CNP can adsorb more CO_2. The enhanced CO_2 adsorption on Rh/CNP might be related to the electronic donation effect from P to Rh, which favored the electron transfer into the anti-bonding orbitals for CO_2 activation [73]. Furthermore, the CO_2 desorption temperature on Rh/CNP shifted towards higher temperature compared with that on Rh/CN, suggesting that stronger adsorption of CO_2 on Rh/CNP, which is beneficial for subsequent hydrogenation process. CO* is considered as an important reaction intermediate via C-C coupling with CH_x * for ethanol production. The generated CO* intermediates may undergo hydrogenation, desorption, or C-C coupling. H_2-D_2 isotopic exchange experiment was conducted to assess the hydrogenation capability of the catalysts. Fig. S16 illustrates that Rh/CNP exhibits a relatively weak ability to catalyze the isotopic exchange of H_2 and D_2. Furthermore, CO-TPD profiles show that Rh/CNP is beneficial for CO adsorption (Fig. S17). Consequently, Rh/CNP may facilitate the stabilization of CO* and limit its subsequent hydrogenation into other by-products

(such as methane and methanol) due to its lower hydrogenation activity. This could promote C-C coupling to produce ethanol. DFT calculations also revealed that CO hydrogenation is more likely to occur on Rh/CN (Fig. S18), indicating that CO* formed on Rh/CN is more facile to hydrogenate into CHO* intermediates for methanol formation. The catalytic performance of the Rh/CN and Rh/CNP catalysts for CO hydrogenation under the same conditions as CO_2 hydrogenation (250 °C, 3 MPa) was conducted (Fig. S19). The relative lower CO conversion further confirms that the CO over Rh/CNP catalyst is difficult to undergo hydrogenation reaction. Notably, the major alcohol product in CO hydrogenation is methanol. It indicates the different hydrogenation behavior between CO_2 and CO, which has been demonstrated in our previous work [27]. Ethanol was only found in Rh/CNP catalyst. However, the yield of ethanol in CO_2 hydrogenation is much higher than that in CO hydrogenation (4.0% vs 0.3%), indicating that ethanol majorly comes from CO_2 hydrogenation instead of CO hydrogenation. The space-time yield (STY) of ethanol on Rh/CNP was up to 3.68 mmol $g^{-1}h^{-1}$, surpassing most of the ever-reported Rh-based catalysts in ethanol formation from CO_2 hydrogenation (Fig. 3b, Table S6).

In addition, the stability of Rh/CN and Rh/CNP were evaluated in five cycles at 250 °C, 3 MPa. The results were given in Figs. 3c and 3d. Both the Rh/CN and Rh/CNP were well reproduced using five runs with the insignificant decreases in activity and methanol/ethanol selectivity. The negligible loss in reactivity may be attributed to incomplete catalyst recovery in each reaction run. The ICP results showed that the Rh and P contents in spent Rh/CNP catalyst remained almost unchanged (Table S1). Next, we conducted XRD, SEM, and TEM characterizations of the spent Rh/CNP catalyst to explore the structural change during reaction. As shown in Figs. S20-S22, the spent Rh/CNP catalyst still maintains the characteristics of graphite-like materials and rhombic dodecahedron-shaped morphology, suggesting the excellent structural stability of the catalyst during reaction. The AC-HAADF-STEM image showed that single-atom Rh can still be observed over spent Rh/CNP (Fig. S23), indicating the structures of Rh single atoms can be maintained for the spent catalyst.

The best catalytic performance of the Rh/CNP catalyst was obtained by adjusting the type and content of solvent, the catalyst dosage, and the Rh loading (Figs. S24-27). The results show that the water exhibited the best catalytic performance among all solvents, and the ethanol selectivity increased significantly as the water volume increased from 0 to 20 mL. Our previous work has confirmed that water took part in the reaction by providing hydrogen source, thus promoting the production of ethanol [45]. In addition, the CO_2 conversion and ethanol selectivity both increased with the Rh/CNP catalyst dosage (Fig. S26). The increase of catalyst dosage naturally promoted CO_2 conversion, which was beneficial for driving the subsequent dissociation of CH₃OH* into CH_3 * and the C-C coupling to form ethanol. Considering that the loading of noble metal is also an important factor, we prepared Rh/CNP catalysts with different Rh loading by adjusting the amount of Rh(NO_3)₃•6 H_2O added. As shown in Fig. S27, it can be seen that the CO_2 conversion increased with the increase of Rh loading, while further increasing Rh loading notably decreased the ethanol selectivity along with the enhanced formation of CO and CH_3OH. This may be attributed to excessive Rh adsorbed more H* , the formed CO* intermediate cannot be effectively consumed for coupling with CH_3 * owing to the presence of more Rh clusters or nanoparticles shifting Rh electronic state from $Rh^{\delta+}$ to metallic Rh, but were more inclined to hydrogenate to form CH_3OH. The activity and products selectivity are sensitive to the temperature and pressure. As shown in Fig. S28, it can be found that higher temperature and higher pressure promote CO_2 hydrogenation to produce ethanol over Rh/CNP. It is reported that high temperature favors methanol dissociation into CH_3 * , whereas low temperature tends to result in the formation of CH_3O* [74]. CH_3 * and CH_3O* are crucial intermediates for the production of ethanol and methanol, respectively. The effect of reaction pressure on catalytic performance is related to reaction thermodynamics as high pressure is beneficial for CO insertion.

Therefore, raising reaction temperature and pressure is beneficial for the generation of ethanol over Rh/CNP. In contrast, at different temperatures and pressures, only methanol is generated over Rh/CN catalysts (Fig. S29). The above results indicate that Rh/CN functions as a highly active and selective catalyst for CH_3OH production in CO_2 hydrogenation, while Rh/CNP is more favorable for ethanol formation. In addition, the effect of reaction time on product selectivity was also considered. As shown in Fig. 3e, the Rh-N_4 sites exhibited increasing methanol selectivity along with decreasing CO selectivity with increase of reaction time. In terms of Rh/CNP, the ethanol selectivity increasing accompanied by the decline in CO and methanol selectivity (Fig. 3f). It implies that ethanol is generated via the C-C coupling between CO and dissociative CH_3 * from methanol on Rh-N_3P_1 sites, while this reaction route could not occur on Rh-N_4 sites.

For a more comprehensive understanding of the reaction process, we conducted a catalytic performance test in a continuous flow-type fixed-bed reactor. As depicted in Fig. S30, the CO_2 conversion on both Rh/CN and Rh/CNP catalysts is very poor, which is related to the low Rh content in the catalysts (0.07 wt% for Rh/CN, 0.09 wt% for Rh/CNP). CO is the main product over the two Rh SACs, suggesting that the single atom sites favor reverse water gas shift reaction (RWGS) in the fixed-bed CO_2 hydrogenation reaction. It is related to the facile desorption of CO* and relative weak hydrogenation ability on the single atom in this reaction system. In addition to CO, some CH_3OH generation was also observed. The gas in the fixed-bed reactor is in a continuous-flow state, the residence time for reactants and reaction intermediates in the fixed-bed reactor is quite limited owing to the high gas hourly space velocity (GHSV), which favors the desorption of primary products (CO and CH_3OH). Interestingly, there was almost no formation of ethanol on both catalysts. It is related to limited residence time of CO and CH_3OH. This also confirms that ethanol is the secondary product in CO_2 hydrogenation, derived from the reaction between CO and CH_3OH. However, it should be noted that fixed-bed reactor and batch reactor are two different reaction systems. In the batch reactor, both reactants and intermediates are in a closed environment with a long residence time, which is conducive to the reaction or C-C coupling of intermediates, thereby promoting the hydrogenation of CO_2 to ethanol.

3.4. Mechanism of CO_2 hydrogenation to ethanol

To elucidate the catalytic mechanism of Rh/CNP in the CO_2 hydrogenation reaction, we conducted in situ DRIFTS by exposing it to a CO_2/H_2 mixture at various temperatures. The assignments for IR bands are determined based on the adsorption infrared spectra of different known species (Fig. S31) and the literatures. As shown in Fig. S32, the band assigned to HCOO* species (1351, 1733 cm^{-1}) can be identified [29, 37], indicating the occurrence of a reaction between adsorbed CO_2 * and chemisorbed hydrogen. When the temperature increased to 100 °C, a weak peak at 2837 cm^{-1} ascribed to CH_3O* appears [75], suggesting that low temperature favors the formation of CH_3OH* . With the temperature increasing, the peak intensity of CH_3O* gradually decrease. The change in CH_3O* peak is not particularly significant, as the formed CH_3O* intermediate is unstable and rapidly dissociates to form CH_3 * (2875 cm^{-1}) [76]. Meanwhile, the peaks ascribed to C_2H_5O* (2916 and 2964 cm^{-1}) were observed starting from 150 °C [77], which originates from the CH_3 * coupling with CO* . For comparison, in situ DRIFTS over Rh/CN catalyst were also conducted to explore the reaction mechanism of CO_2 hydrogenation into methanol. Fig. S33 shows the DRIFTS spectra of Rh/CN in the region of 3100–2600 cm^{-1} and 2000–1000 cm^{-1} at different temperatures. The bands located at 2976, 2877, 2750, 1738, and 1540 cm^{-1} are attributed to HCOO* species, while the bands at 2929, 2750, and 1135 cm^{-1} correspond to CH_3O* species. It is evident that the peak intensity of CH_3O* species significantly increases with the temperature, indicating that the formation of methanol.

Density functional theory (DFT) calculations were conducted to gain a deeper understanding of the reaction mechanism, identifying potential

intermediates and examining them to construct a plausible thermodynamic reaction pathway. In CO_2 hydrogenation, the initial step involves the adsorption and activation of CO_2. The most favorable pathway for CO formation is the RWGS reaction through COOH* intermediate and its subsequent dissociation (Figs. S34-36). The adsorbed CO_2 can also be hydrogenated into HCOO* , which is an important intermediate that could further be hydrogenated into H_2COO* and HCOOH* over Rh/CNP model (Fig. S37). H exhibits a preference to bond with C to form H_2COO* due to the free energy for H_2COO* formation (0.28 eV) is slightly lower than that for HCOOH* (0.30 eV). Additionally, the cleavage of the C-O bond in H_2COO* is more favorable in comparison to that in HCOOH* (0.38 vs 0.97 eV, Fig. 4a and Fig. S37). The formed CH_2O* from H_2COO* dissociation could be further hydrogenated into CH_2OH* and CH_3OH* . The energy barrier for C-O bond cleavage in CH_2OH* is higher than that in CH_3OH* (0.93 eV vs 0.27 eV), indicating that the pathway for the dissociation of CH_3OH* into CH_3 * is more facile. The resulting CH_3 * can undergo coupling with CO* to produce CH_3CO* , which then undergoes a multi-step hydrogenation process to yield ethanol. The energy profiles and the structures of reaction intermediates are illustrated in Fig. 4a and Fig. S38. Notably, the energy barrier for C-C coupling is only 0.48 eV, significantly lower than that for CO desorption (1.63 eV, as shown in Fig. S34) or hydrogenation (2.96 eV, Fig. S18). This means that formed CO* on Rh/CNP is more likely to be consumed for C-C coupling. Moreover, the possibility of C-C coupling between CH_3 * and CO_2 * /HCOO* was also considered (Figs. S39 and S40). The calculated energy barriers for the mentioned routes are 2.24 and 1.66 eV, respectively, significantly higher than the energy barrier with CO* (0.48 eV). This further proves that the formation of ethanol over Rh/CNP follows the CO insert mechanism. By contrast, the reaction pathway for CO_2 hydrogenation over Rh/CN is also considered. The adsorbed CO_2 could be initially hydrogenated into COOH* (Figs. S35 and S36) or HCOO* (Figs. S41 and S42), followed by further hydrogenation into CH_3OH* . The free energies for rate determining step in these two routes are calculated to be 1.50 and 1.12 eV, respectively, suggesting that the HCOO* intermediated route is more energetically favorable. According to DFT calculations, a high energy barrier of 2.33 eV is observed for the dissociation of CH_3OH* into CH_3 * over the Rh/CN model (Fig. 4b). It suggests that ethanol is hardly formed through methanol dissociation over Rh/CN catalyst.

To prove this standpoint, CO hydrogenation reaction using methanol as co-feeding was performed (Fig. 4c). As mentioned above, minor ethanol along with major methanol was generated in CO hydrogenation over Rh/CNP catalyst, while only methanol was produced as liquid product for Rh/CN catalyst. When methanol was presented as co-feeding with CO/H_2, the ethanol production was enhanced significantly, along with the consumption of methanol over Rh/CNP catalyst. This indicates the existence of reaction pathway from methanol and CO to ethanol. Therefore, in CO_2 hydrogenation, ethanol is generated via the C-C coupling between CO and methanol on Rh-N_3P_1 sites. However, the Rh-N_4 sites do not have this ability, possibly owing to the weak ability for C-O bonds dissociation. In order to further check this viewpoint, the long chain alcohols (ethanol and propanol) as co-feeding with CO/H_2 were carried out. As shown in Fig. 4c, the Rh-N_4 sites still did not exhibit any conversion of ethanol or propanol, accompanied with no production of propanol or butanol. However, Rh-N_3P_1 sites showed the production of propanol and butanol along with evident consumption of ethanol and propanol, respectively. This result confirms the characteristic ability for C-O bond breaking on the Rh-N_3P_1 sites, which contributes to the formation of CH_x * and its subsequent C-C coupling with CO* to form ethanol in CO_2 hydrogenation reaction. By contrast, the weak ability for C-O bond breaking on the Rh-N_4 sites results in methanol as the major product in CO_2 hydrogenation reaction. Additionally, with the increase of carbon number from 1 to 3, the conversion of alcohols (ROH) and STY value for longer-chain alcohol product decrease, possibly owing to the stronger steric hindrance effects from the longer carbon chain in ROH. Obvious methanol conversion and ethanol formation can also be
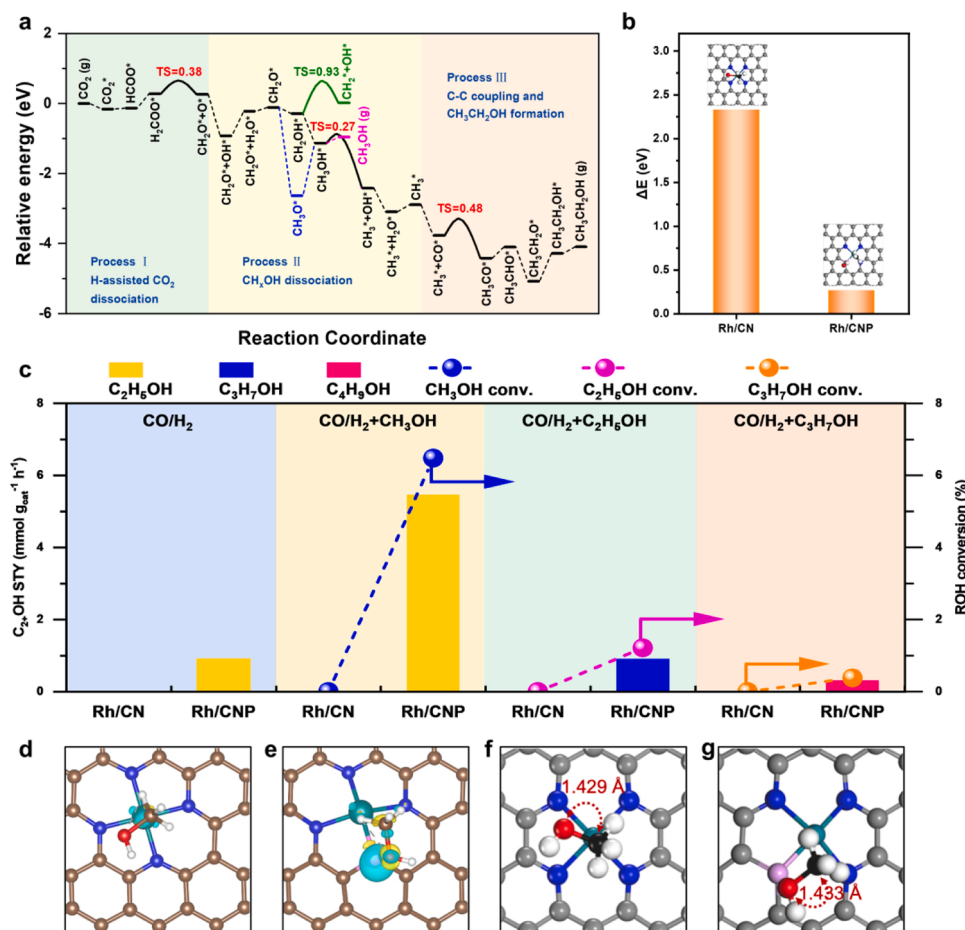
Fig. 4. (a) DFT free-energy diagram of the CO_2 hydrogenation process over Rh/CNP catalyst model, (b) A comparison of the energy barrier for CH_3OH^* dissociation between the Rh/CN and Rh/CNP models, (c) Catalytic performance of the catalysts under CO/H_2 atmosphere, reaction conditions: 30 mg catalyst, 20 mL H_2O, initial pressure 3.0 MPa ($H_2/CO=2:1$), 250 °C, 5 h, 10 mmol methanol/ethanol/propanol used for co-feeding, Charge density difference of CH_3OH^* adsorption over Rh/CN (d) and Rh/CNP (e) model. The yellow and cyan colors represent the accumulation and depletion of electron density, respectively, with an iso-surface value set at 0.001 e/bohr^3. Rh atoms in dark cyan; C atoms in brown; N atoms in blue; P atoms in pink; O atoms in red; H atoms in white, and the calculated length of C-O bond in CH_3OH^* over Rh/CN (f) and Rh/CNP (g) model. Rh atoms in dark cyan; C atoms in gray; N atoms in blue; P atoms in pink; C atoms in CH_3OH^* in black; O atoms in red; H atoms in white.

observed on the other M-N_3P_1 sites compared with no methanol conversion on the M-N_4 sites (M=Pd, Ir, Co, and Cu) (Fig. S43), indicating that the promoting effect of P on the C-O bond breaking ability in CH_3OH is universal.

The formation of ethanol was attributed to the C-C coupling between CO^* and CH_3^* species derived from CH_3OH^* dissociation. The above results evidenced that Rh-N_3P_1 and Rh-N_4 sites exhibited diverse catalytic behaviors derived from their different ability to activate CH_3OH^* dissociation. On the other hand, Rh-N_4 sites may be deficient for the C-C coupling between CH_3^* and CO^*, leading to Rh-N_4 sites being unfavorable for generating ethanol. To confirm whether catalyst C-C coupling ability determines the product selectivity, we also performed the hydroformylation reaction using CO/H_2/1-hexene as reactants (Fig. S44). Both the catalysts have shown heptanal formation along with 1-hexene and CO consumption, suggesting the existence of strong C-C coupling ability on both two catalysts. Combined with above model experiment results, it concludes that the reason for the significant different product selectivity in CO_2 hydrogenation on Rh-N_4 sites and Rh-N_3P_1 sites is not attributed to the different C-C coupling ability, but rather the different C-O bond cleavage ability for the supply of CH_x^*. Even Rh-N_4 sites could catalyze the coupling between CH_3^* and CO, the deficient supply in CH_3^* contributes to no ethanol production in CO_2 hydrogenation.

Apparently, it is related to the introduction of P with strong eletronic

donation ability. According to charge density difference of CH_3OH^* adsorption (Figs. 4d and 4e), the electron distribution on Rh/CN and Rh/CNP catalysts is quite different. The adsorption of CH_3OH^* on Rh/CN did not exhibit significant charge density difference. However, after the doption of P, clear electron donation from P atom to the O and C atoms in CH_3OH^* was found. Based on the Bader charge changes of CH_3OH^* adsorption (Table S7), the number of C-O electrons on Rh/CN is lower than that on Rh/CNP (0.7213 e vs 0.7934 e), indicating that the C-O bond of Rh/CNP is easily activated and likely to be broken. In addition, the calculated length of C-O bond in CH_3OH^* is presented in Figs. 4f and 4g. The Rh/CNP adsorbed CH_3OH^* exhibited longer C-O bond length than that for Rh/CN (1.433 Å vs 1.429 Å), further proving that the weakened C-O bond in CH_3OH^* after P doping. In conclusion, this work has revealed a novel catalysis mechanism of P doping for ethanol production from CO_2 hydrogenation, as summarized in Scheme 1.

4. Conclusions

In summary, Rh/CN catalyst with Rh-N_4 sites was prepared through the pyrolysis of Rh-containing MOFs, and the Rh/CNP catalyst with Rh-N_3P_1 sites was rationally designed by phosphorus-substitution of atomically dispersed Rh-N_4 sites. The resulting catalysts have shown significantly different catalytic performance in CO_2 hydrogenation. Rh/
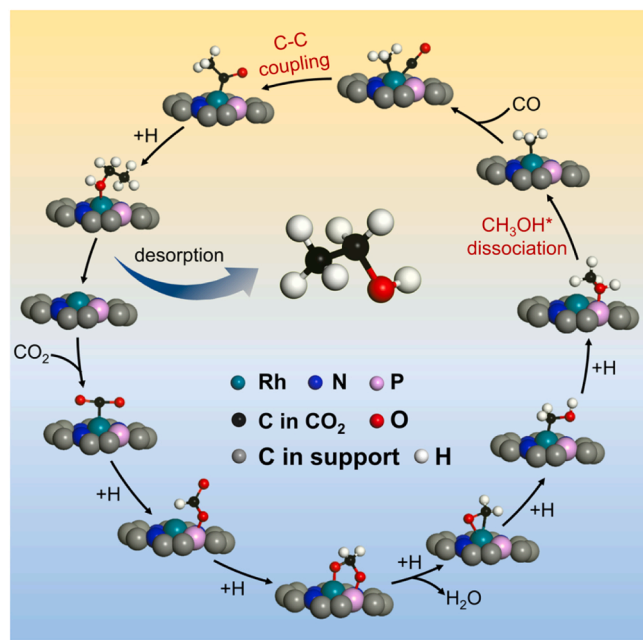
Scheme 1. Proposed reaction mechanism for ethanol production from CO_2 hydrogenation over Rh/CNP catalyst.

CN catalyst exhibited a high selectivity to methanol (91.3%), while Rh/CNP catalyst facilitated ethanol production with a selectivity of 81.8% and a TOF of 420.7 h^{-1}, ranking high among the ever-reported catalysts in ethanol production from CO_2 hydrogenation. Detailed experimental results combined with DFT calculations revealed that the substitution of P in Rh-N_4 sites could effectively weaken the C-O bonds in CH_3OH^* intermediate through electronic donation effect, which largely reduces the energy barrier for CH_3 * formation from CH_3OH^* dissociation. The enhanced supply of CH_3 * is favorable for the subsequent C-C coupling with CO* to generate $C_2H_5OH^*$. By contrast, the activation of methanol is more challenging on the Rh-N_4 sites, resulting in methanol as major product. This work not only provides an efficient site-pair catalytic system for highly selective ethanol formation in CO_2 hydrogenation, but also provides a fundamental understanding of the relationship between coordination environment and catalytic performance. These findings could also serve as valuable guidance for rational design of the other high-efficency site-pair catalysis for various reactions.

CRediT authorship contribution statement

Zheng Ke: Writing – original draft, Investigation, Formal analysis, Data curation, Conceptualization. **Li Yufeng:** ormal analysis, Data curation. **Liu Bing:** ormal analysis, Data curation. **Chen Jie:** Data curation. **Xu Yuebing:** Data curation. **Li Zaijun:** Data curation. **Liu Xiaohao:** Supervision, Methodology, Writing – review & editing, Conceptualization, Validation, Project administration, Funding acquisition.

Declaration of Competing Interest

The authors declare that they have no known competing financial interests or personal relationships that could have appeared to influence the work reported in this paper.

Data availability

The data that support the findings of this study are available from the corresponding author upon reasonable request.

Acknowledgements

Appendix A. Supporting information

Supplementary data associated with this article can be found in the online version at doi:10.1016/j.apcatb.2024.123730.

References

[1] S. Ren, D. Joulié, D. Salvatore, K. Torbensen, M. Wang, M. Robert, C. P. Berlinguette, Molecular electrocatalysts can mediate fast, selective CO_2 reduction in a flow cell, Science 365 (2019) 367–369.

[2] R.-P. Ye, J. Ding, W. Gong, M.D. Argyle, Q. Zhong, Y. Wang, C.K. Russell, Z. Xu, A. G. Russell, Q. Li, M. Fan, Y.-G. Yao, CO_2 hydrogenation to high-value products via heterogeneous catalysis, Nat. Commun. 10 (2019) 5698.

[3] Y. Jiang, Y. Sung, C. Choi, G. Joo Bang, S. Hong, X. Tan, T.-S. Wu, Y.-L. Soo, P. Xiong, M. Meng-Jung Li, L. Hao, J. Jung, Z. Sun, Single-atom molybdenum-N_3 sites for selective hydrogenation of CO_2 to CO, Angew. Chem. Int. Ed. 61 (2022) e202203836.

[4] Y. Li, Z. Zhao, W. Lu, H. Zhu, F. Sun, B. Mei, Z. Jiang, Y. Lyu, X. Chen, L. Guo, T. Wu, X. Ma, Y. Meng, Y. Ding, Single-atom Co-N-C catalysts for high-efficiency reverse water-gas shift reaction, Appl. Catal. B Environ. 324 (2023) 122298.

[5] B. Dai, S. Cao, H. Xie, G. Zhou, S. Chen, Reduction of CO_2 to CO via reverse water-gas shift reaction over CeO_2 catalyst, , Korean J. Chem. Eng. 35 (2018) 421–427.

[6] F. Wang, S. He, H. Chen, B. Wang, L. Zheng, M. Wei, D.G. Evans, X. Duan, Active site dependent reaction mechanism over Ru/CeO_2 catalyst toward CO_2 methanation, J. Am. Chem. Soc. 138 (2016) 6298–6305.

[7] W. Li, A. Zhang, X. Jiang, C. Chen, Z. Liu, C. Song, X. Guo, Low temperature CO_2 methanation: ZIF-67-derived Co-based porous carbon catalysts with controlled crystal morphology and size, ACS Sustain. Chem. Eng. 5 (2017) 7824–7831.

[8] Y. Zhao, V. Girelli, O. Ersen, D.P. Debecker, CO_2 methanation with high-loading mesoporous Ni/SiO_2 catalysts: toward high specific activity and new mechanistic insights, J. Catal. 426 (2023) 283–293.

[9] X. Liu, M. Wang, C. Zhou, W. Zhou, K. Cheng, J. Kang, Q. Zhang, W. Deng, Y. Wang, Selective transformation of carbon dioxide into lower olefins with a bifunctional catalyst composed of $ZnGa_2O_4$ and SAPO-34, Chem. Commun. 54 (2018) 140–143.

[10] L. Wang, Y. Han, J. Wei, Q. Ge, S. Lu, Y. Mao, J. Sun, Dynamic confinement catalysis in Fe-based CO_2 hydrogenation to light olefins, Appl. Catal. B Environ. 328 (2023) 122506.

[11] B. Liu, S. Geng, J. Zheng, X. Jia, F. Jiang, X. Liu, Unravelling the new roles of Na and Mn promoter in CO_2 hydrogenation over Fe_3O_4-based catalysts for enhanced selectivity to light α-olefins, ChemCatChem 10 (2018) 4718–4732.

[12] Y. Ni, Z. Chen, Y. Fu, Y. Liu, W. Zhu, Z. Liu, Selective conversion of CO_2 and H_2 into aromatics, Nat. Commun. 9 (2018) 3457.

[13] Y. Wang, L. Tan, M. Tan, P. Zhang, Y. Fang, Y. Yoneyama, G. Yang, N. Tsubaki, Rationally designing bifunctional catalysts as an efficient strategy to boost CO_2 hydrogenation producing value-added aromatics, ACS Catal. 9 (2019) 895–901.

[14] Y. Xu, C. Shi, B. Liu, T. Wang, J. Zheng, W. Li, D. Liu, X. Liu, Selective production of aromatics from CO_2, Catal. Sci. Technol. 9 (2019) 593–610.

[15] H. Zhou, Z. Chen, A.V. López, E.D. López, E. Lam, A. Tsoukalou, E. Willinger, D. A. Kuznetsov, D. Mance, A. Kierzkowska, F. Donat, P.M. Abdala, A. Comas-Vives, C. Copéret, A. Fedorov, C.R. Müller, Engineering the Cu/Mo_2CT_x (MXene) interface to drive CO_2 hydrogenation to methanol, Nat. Catal. 4 (2021) 860–871.

[16] Z. Cai, M. Huang, J. Dai, G. Zhan, F.-l. Sun, G.-L. Zhuang, Y. Wang, P. Tian, B. Chen, S. Ullah, J. Huang, Q. Li, Fabrication of Pd/In_2O_3 nanocatalysts derived from MIL-68(In) loaded with molecular metalloporphyrin (TCPP(Pd)) toward CO_2 hydrogenation to methanol, ACS Catal. 12 (2022) 709–723.

[17] F. Studt, I. Sharafutdinov, F. Abild-Pedersen, C.F. Elkjær, J.S. Hummelshøj, S. Dahl, I. Chorkendorff, J.K. Nørskov, Discovery of a Ni-Ga catalyst for carbon dioxide reduction to methanol, Nat. Chem. 6 (2014) 320–324.

[18] F. Jiang, S. Wang, B. Liu, J. Liu, L. Wang, Y. Xiao, Y. Xu, X. Liu, Insights into the influence of CeO_2 crystal facet on CO_2 hydrogenation to methanol over Pd/CeO_2 Catalysts, ACS Catal. 10 (2020) 11493–11509.

[19] W. Tu, P. Ren, Y. Li, Y. Yang, Y. Tian, Z. Zhang, M. Zhu, Y.-H.C. Chin, J. Gong, Y.-F. Han, Gas-dependent active sites on Cu/ZnO clusters for CH_3OH synthesis, J. Am. Chem. Soc. 145 (2023) 8751–8756.

[20] D. Xu, M. Ding, X. Hong, G. Liu, S.C.E. Tsang, Selective C_{2+} alcohol synthesis from direct CO_2 hydrogenation over a Cs-promoted Cu-Fe-Zn catalyst, ACS Catal. 10 (2020) 5250–5260.

[21] X. Zhou, C. Wang, Y. Chu, J. Xu, Q. Wang, G. Qi, X. Zhao, N. Feng, F. Deng, Observation of an oxonium ion intermediate in ethanol dehydration to ethene on zeolite, Nat. Commun. 10 (2019) 1961.

[22] J.E. van den Reijen, S. Kanungo, T.A.J. Welling, M. Versluijs-Helder, T.A. Nijhuis, K.P. de Jong, P.E. de Jongh, Preparation and particle size effects of Ag/α-Al$_2$O$_3$ catalysts for ethylene epoxidation, J. Catal. 356 (2017) 65–74.

[23] A. Dokania, A. Ramírez, A. Bavykina, J. Gascon, Heterogeneous catalysis for the valorization of CO$_2$: role of bifunctional processes in the production of chemicals, ACS Energy Lett. 4 (2019) 167–176.

[24] S.S. Ali, S.S. Ali, N. Tabassum, A review on CO$_2$ hydrogenation to ethanol: reaction mechanism and experimental studies, J. Environ. Chem. Eng. 10 (2022) 106962.

[25] T.N. Nguyen, J. Guo, A. Sachindran, F. Li, A. Seifitokaldani, C.-T. Dinh, Electrochemical CO$_2$ reduction to ethanol: from mechanistic understanding to catalyst design, J. Mater. Chem. A 9 (2021) 12474–12494.

[26] Y. Song, W. Chen, W. Wei, Y. Sun, Advances in clean fuel ethanol production from electro-, photo- and photoelectro-catalytic CO$_2$ reduction, Catalysts (2020).

[27] J. Chen, Y. Zha, B. Liu, Y. Li, Y. Xu, X. Liu, Rationally designed water enriched nano reactor for stable CO$_2$ hydrogenation with near 100% ethanol selectivity over diatomic palladium active sites, ACS Catal. 13 (2023) 7110–7121.

[28] Y. Lou, F. jiang, W. Zhu, L. Wang, T. Yao, S. Wang, B. Yang, B. Yang, Y. Zhu, X. Liu, CeO$_2$ supported Pd dimers boosting CO$_2$ hydrogenation to ethanol, Appl. Catal. B Environ. 291 (2021) 120122.

[29] F. Zhang, W. Zhou, X. Xiong, Y. Wang, K. Cheng, J. Kang, Q. Zhang, Y. Wang, Selective hydrogenation of CO$_2$ to ethanol over sodium-modified rhodium nanoparticles embedded in zeolite silicalite-1, J. Phys. Chem. C 125 (2021) 24429–24439.

[30] L. Wang, S. He, L. Wang, Y. Lei, X. Meng, F.-S. Xiao, Cobalt-nickel catalysts for selective hydrogenation of carbon dioxide into ethanol, ACS Catal. 9 (2019) 11335–11340.

[31] H. Zhang, H. Han, L. Xiao, W. Wu, Highly selective synthesis of ethanol via CO$_2$ hydrogenation over CoMoC$_x$ Catalysts, ChemCatChem 13 (2021) 3333–3339.

[32] A.H.M. da Silva, L.H. Vieira, C.S. Santana, M.T.M. Koper, E.M. Assaf, J.M. Assaf, J. F. Gomes, Ethanol formation from CO$_2$ hydrogenation at atmospheric pressure using Cu catalysts: water as a key component, Appl. Catal. B Environ. 324 (2023) 122221.

[33] J. Huang, G. Zhang, J. Zhu, M. Wang, F. Ding, C. Song, X. Guo, Boosting the production of higher alcohols from CO$_2$ and H$_2$ over Mn- and K-modified iron carbide, Ind. Eng. Chem. Res. (2022).

[34] X. Xi, F. Zeng, H. Zhang, X. Wu, J. Ren, T. Bisswanger, C. Stampfer, J.P. Hofmann, R. Palkovits, H.J. Heeres, CO$_2$ hydrogenation to higher alcohols over K-promoted bimetallic Fe-In catalysts on a Ce-ZrO$_2$ support, ACS Sustain. Chem. Eng. 9 (2021) 6235–6249.

[35] Q. Zhang, S. Wang, R. Geng, P. Wang, M. Dong, J. Wang, W. Fan, Hydrogenation of CO$_2$ to higher alcohols on an efficient Cr-modified CuFe catalyst, Appl. Catal. B Environ. 337 (2023) 123013.

[36] Y. Wang, K. Wang, B. Zhang, X. Peng, X. Gao, G. Yang, H. Hu, M. Wu, N. Tsubaki, Direct conversion of CO$_2$ to ethanol boosted by intimacy-sensitive multifunctional catalysts, ACS Catal. 11 (2021) 11742–11753.

[37] D. Xu, H. Yang, X. Hong, G. Liu, S.C. EdmanTsang, Tandem catalysis of direct CO$_2$ hydrogenation to higher alcohols, ACS Catal. 11 (2021) 8978–8984.

[38] G. Wang, R. Luo, C. Yang, J. Song, C. Xiong, H. Tian, Z.-J. Zhao, R. Mu, J. Gong, Active sites in CO$_2$ hydrogenation over confined VO$_x$-Rh catalysts, Sci. China Chem. 62 (2019) 1710–1719.

[39] C. Yang, R. Mu, G. Wang, J. Song, H. Tian, Z.J. Zhao, J. Gong, Hydroxyl-mediated ethanol selectivity of CO$_2$ hydrogenation, Chem. Sci. 10 (2019) 3161–3167.

[40] H. Kusama, K. Okabe, K. Sayama, H. Arakawa, CO$_2$ hydrogenation to ethanol over promoted Rh/SiO$_2$ catalysts, Am. J. Trop. Med. Hyg. 73 (1996) 815–819.

[41] B. Singh, V. Sharma, R.P. Gaikwad, P. Fornasiero, R. Zbořil, M.B. Gawande, Single-atom catalysts: a sustainable pathway for the advanced catalytic applications, Small 17 (2021) 2006473.

[42] K. Wang, B. Chen, Y. Xuan, W. Fan, N. Sun, S. Chang, G. Meng, Efficient utilization of nickel single atoms for CO$_2$ electroreduction by constructing 3D interconnected nitrogen-doped carbon tube network, Appl. Catal. B Environ. 338 (2023) 123083.

[43] Z. Yu, Y. Li, A. Torres-Pinto, A.P. LaGrow, V.M. Diaconescu, L. Simonelli, M. J. Sampaio, O. Bondarchuk, I. Amorim, A. Araujo, A.M.T. Silva, C.G. Silva, J. L. Faria, L. Liu, Single-atom Ir and Ru anchored on graphitic carbon nitride for efficient and stable electrocatalytic/photocatalytic hydrogen evolution, Appl. Catal. B Environ. 310 (2022) 121318.

[44] Q. Wang, X. Zheng, J. Wu, Y. Wang, D. Wang, Y. Li, Recent progress in thermal conversion of CO$_2$ via single-Atom site catalysis, Small Struct. 3 (2022) 2200059.

[45] K. Zheng, Y. Li, B. Liu, F. Jiang, Y. Xu, X. Liu, Ti-doped CeO$_2$ stabilized single-atom rhodium catalyst for selective and stable CO$_2$ hydrogenation to ethanol, Angew. Chem. Int. Ed. 61 (2022) e202210991.

[46] X. Ye, C. Yang, X. Pan, J. Ma, Y. Zhang, Y. Ren, X. Liu, L. Li, Y. Huang, Highly selective hydrogenation of CO$_2$ to ethanol via designed bifunctional Ir$_1$-In$_2$O$_3$ single-atom catalyst, J. Am. Chem. Soc. 142 (2020) 19001–19005.

[47] F.J. Caparrós, L. Soler, M.D. Rossell, I. Angurell, L. Piccolo, O. Rossell, J. Llorca, Remarkable carbon dioxide hydrogenation to ethanol on a palladium/iron oxide single-atom catalyst, ChemCatChem 10 (2018) 2365–2369.

[48] L. Wang, J. Wu, S. Wang, H. Liu, Y. Wang, D. Wang, The reformation of catalyst: from a trial-and-error synthesis to rational design, Nano Res. (2023) 1–41.

[49] Z. Mo, D. Tai, H. Zhang, A. Shahab, A comprehensive review on the adsorption of heavy metals by zeolite imidazole framework (ZIF-8) based nanocomposite in water, Chem. Eng. J. 443 (2022) 136320.

[50] Z. Li, Y. Chen, S. Ji, Y. Tang, W. Chen, A. Li, J. Zhao, Y. Xiong, Y. Wu, Y. Gong, T. Yao, W. Liu, L. Zheng, J. Dong, Y. Wang, Z. Zhuang, W. Xing, C.-T. He, C. Peng, W.-C. Cheong, Q. Li, M. Zhang, Z. Chen, N. Fu, X. Gao, W. Zhu, J. Wan, J. Zhang, L. Gu, S. Wei, P. Hu, J. Luo, J. Li, C. Chen, Q. Peng, X. Duan, Y. Huang, X.-M. Chen, D. Wang, Y. Li, Iridium single-atom catalyst on nitrogen-doped carbon for formic acid oxidation synthesized using a general host–guest strategy, Nat. Chem. 12 (2020) 764–772.

[51] Y. Chen, S. Ji, Y. Wang, J. Dong, W. Chen, Z. Li, R. Shen, L. Zheng, Z. Zhuang, D. Wang, Y. Li, Isolated single iron atoms anchored on N-doped porous carbon as an efficient electrocatalyst for the oxygen reduction reaction, Angew. Chem. Int. Ed. 56 (2017) 6937–6941.

[52] T. Gan, D. Wang, Atomically dispersed materials: ideal catalysts in atomic era, Nano Res. (2023) 1–21.

[53] T. Yang, X. Mao, Y. Zhang, X. Wu, L. Wang, M. Chu, C.-W. Pao, S. Yang, Y. Xu, X. Huang, Coordination tailoring of Cu single sites on C$_3$N$_4$ realizes selective CO$_2$ hydrogenation at low temperature, Nat. Commun. 12 (2021) 6022.

[54] Y. Dai, H. Li, C. Wang, W. Xue, M. Zhang, D. Zhao, J. Xue, J. Li, L. Luo, C. Liu, X. Li, P. Cui, Q. Jiang, T. Zheng, S. Gu, Y. Zhang, J. Xiao, C. Xia, J. Zeng, Manipulating local coordination of copper single atom catalyst enables efficient CO$_2$-to-CH$_4$ conversion, Nat. Commun. 14 (2023) 3382.

[55] D. Cao, H. Xu, H. Li, C. Feng, J. Zeng, D. Cheng, Volcano-type relationship between oxidation states and catalytic activity of single-atom catalysts towards hydrogen evolution, Nat. Commun. 13 (2022) 5843.

[56] J. Li, M. Li, N. An, S. Zhang, Q. Song, Y. Yang, J. Li, X. Liu, Boosted ammonium production by single cobalt atom catalysts with high Faradic efficiencies, PNAS 119 (2022) e2123450119.

[57] D. Li, C. Wen, J. Huang, J. Zhong, P. Chen, H. Liu, Z. Wang, Y. Liu, W. Lv, G. Liu, High-efficiency ultrathin porous phosphorus-doped graphitic carbon nitride nanosheet photocatalyst for energy production and environmental remediation, Appl. Catal. B Environ. 307 (2022) 121099.

[58] G. Kresse, J. Furthmüller, Efficient iterative schemes for ab initio total-energy calculations using a plane-wave basis set, Phys. Rev. B 54 (1996) 11169–11186.

[59] P.E. Blöchl, Projector augmented-wave method, Phys. Rev. B 50 (1994) 17953–17979.

[60] J.P. Perdew, K. Burke, M. Ernzerhof, Generalized gradient approximation made simple, Phys. Rev. Lett. 77 (1996) 3865–3868.

[61] G. Henkelman, B.P. Uberuaga, H. Jónsson, A climbing image nudged elastic band method for finding saddle points and minimum energy paths, J. Chem. Phys. 113 (2000) 9901–9904.

[62] W. Xie, K. Li, X.-H. Liu, X. Zhang, H. Huang, P-mediated Cu–N$_4$ sites in carbon nitride realizing CO$_2$ photoreduction to C$_2$H$_4$ with selectivity modulation, Adv. Mater. 35 (2023) 2208132.

[63] S. Chen, X. Li, C.-W. Kao, T. Luo, K. Chen, J. Fu, C. Ma, H. Li, M. Li, T.-S. Chan, M. Liu, Unveiling the proton-feeding effect in sulfur-doped Fe–N–C single-atom catalyst for enhanced CO$_2$ electroreduction, Angew. Chem. Int. Ed. 61 (2022) e202206233.

[64] B. Ni, R. Chen, L. Wu, X. Xu, C. Shi, P. Sun, T. Chen, Optimized enhancement effect of sulfur in Fe–N–S codoped carbon nanosheets for efficient oxygen reduction reaction, ACS Appl. Mater. Interfaces 12 (2020) 23995–24006.

[65] X. Yang, K. Li, D. Cheng, W.-L. Pang, J. Lv, X. Chen, H.-Y. Zang, X.-L. Wu, H.-Q. Tan, Y.-H. Wang, Y.-G. Li, Nitrogen-doped porous carbon: highly efficient trifunctional electrocatalyst for oxygen reversible catalysis and nitrogen reduction reaction, J. Mater. Chem. A 6 (2018) 7762–7769.

[66] H. Funke, A.C. Scheinost, M. Chukalina, Wavelet analysis of extended X-ray absorption fine structure data, Phys. Rev. B 71 (2005) 094110.

[67] Y. Kwon, T.Y. Kim, G. Kwon, J. Yi, H. Lee, Selective activation of methane on single-atom catalyst of rhodium dispersed on zirconia for direct conversion, J. Am. Chem. Soc. 139 (2017) 17694–17699.

[68] R. Lang, T. Li, D. Matsumura, S. Miao, Y. Ren, Y.-T. Cui, Y. Tan, B. Qiao, L. Li, A. Wang, X. Wang, T. Zhang, Hydroformylation of olefins by a rhodium single-atom catalyst with activity comparable to RhCl(PPh$_3$)$_3$, Angew. Chem. Int. Ed. 55 (2016) 16054–16058.

[69] J. Wan, Z. Zhao, H. Shang, B. Peng, W. Chen, J. Pei, L. Zheng, J. Dong, R. Cao, R. Sarangi, Z. Jiang, D. Zhou, Z. Zhuang, J. Zhang, D. Wang, Y. Li, In situ phosphatizing of triphenylphosphine encapsulated within metal–organic frameworks to design Atomic Co$_1$–P$_1$N$_3$ interfacial structure for promoting catalytic performance, J. Am. Chem. Soc. 142 (2020) 8431–8439.

[70] J. Ran, T.Y. Ma, G. Gao, X.-W. Du, S.Z. Qiao, Porous P-doped graphitic carbon nitride nanosheets for synergistically enhanced visible-light photocatalytic H$_2$ production, Energy Environ. Sci. 8 (2015) 3708–3717.

[71] S. Liu, H. Zhu, W. Yao, K. Chen, D. Chen, One step synthesis of P-doped g-C$_3$N$_4$ with the enhanced visible light photocatalytic activity, Appl. Surf. Sci. 430 (2018) 309–315.

[72] Q. Wang, T. Ina, W.-T. Chen, L. Shang, F. Sun, S. Wei, D. Sun-Waterhouse, S. G. Telfer, T. Zhang, G.I.N. Waterhouse, Evolution of Zn(II) single atom catalyst sites during the pyrolysis-induced transformation of ZIF-8 to N-doped carbons, Sci. Bull. 65 (2020) 1743–1751.

[73] G.S. Hwang, H.M. Stowe, E. Paek, D. Manogaran, Reaction mechanisms of aqueous monoethanolamine with carbon dioxide: a combined quantum chemical and molecular dynamics study, Phys. Chem. Chem. Phys. 17 (2015) 831–839.

[74] T. Kato, S.-Y. Kang, X. Xu, T. Yamabe, Possible dissociative adsorption of CH$_3$OH and CH$_3$NH$_2$ on Si(100)-2 × 1 surface, J. Phys. Chem. B 105 (2001) 10340–10347.

[75] G. Zhang, G. Fan, L. Zheng, F. Li, Ga-promoted CuCo-based catalysts for efficient CO$_2$ hydrogenation to ethanol: the key synergistic role of Cu-CoGaO$_x$ Interfacial sites, ACS Appl. Mater. Interfaces 14 (2022) 35569–35580.

[76] Y. Li, K. Zheng, Y. Shen, M. Huang, B. Liu, Y. Xu, X. Liu, Acetic acid production from CH$_4$ and CO$_2$ via synergistic catalysis between Pd particles and oxygen vacancies generated in ZrO$_2$, J. Phys. Chem. C 127 (2023) 5841–5854.

[77] J.V. Ochoa, C. Trevisanut, J.-M.M. Millet, G. Busca, F. Cavani, In situ DRIFTS-MS study of the anaerobic oxidation of ethanol over spinel mixed oxides, J. Phys. Chem. C 117 (2013) 23908–23918.